Chemical Engineering Journal 339 (2018) 97–107

Contents lists available at ScienceDirect

Chemical Engineering Journal

journal homepage: www.elsevier.com/locate/cej

# Iron diselenide combined with hollow graphitic carbon nanospheres as a high-performance anode material for sodium-ion batteries

Jin-Sung Park[a], Sun Young Jeong[b], Kyung Min Jeon[a], Yun Chan Kang[a,*], Jung Sang Cho[b,*]

[a] Department of Materials Science and Engineering, Korea University, Anam-Dong, Seongbuk-Gu, Seoul 136-713, Republic of Korea
[b] Department of Engineering Chemistry, Chungbuk National University, Chungbuk 361-763, Republic of Korea

## HIGHLIGHTS

- Scalable synthesis of iron diselenide nanoparticles composited with hollow graphitic carbon nanospheres is presented.
- $FeSe_2$-graphitic carbon composite shows discharge capacity of 425 mA h $g^{-1}$ after 100 cycles.
- Excellent electrochemical performances of composite are attributed to both ultrafine $FeSe_2$ and graphitic carbon.

## GRAPHICAL ABSTRACT

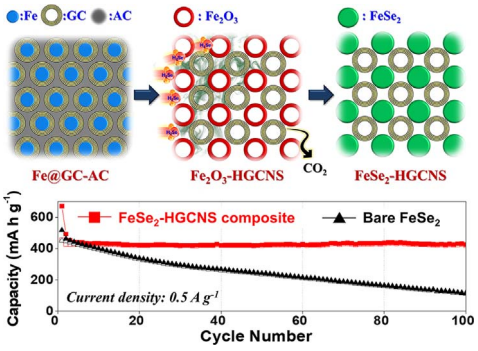


## ARTICLE INFO

*Keywords:*
Iron diselenide
Carbon composite
Graphitic carbon
Anode material
Sodium-ion battery

## ABSTRACT

A scalable method for the synthesis of iron diselenide ($FeSe_2$) nanoparticles composited with hollow graphitic-carbon nanospheres (HGCNS) is presented. The resultant composite exhibits high sodium-ion-storage performance. A solution of iron acetylacetonate, polystyrene, and polyacrylonitrile dissolved in dimethylformamide is subjected to three continuous heat treatment steps. During this process, the amorphous carbon formed around the Fe species in the composite is selectively transformed into graphitic carbon by the catalytic action of the Fe. Residual amorphous carbon was selectively removed. Subsequent selenization of this carbonaceous material affords $FeSe_2$-HGCNS composite. The discharge capacity of this composite is 425 mA h $g^{-1}$ after 100 cycles at a current density of 0.5 A $g^{-1}$, and its capacity retention compared to that in the third cycle is 94%. The excellent sodium-ion-storage performance of the composite is attributed to both ultrafine $FeSe_2$ and HGCNS, which decrease $Na^+$ ion diffusion length, increase electrical conductivity and allow easy penetration of the electrolyte.

## 1. Introduction

Na-ion batteries (NIBs) present a feasible alternative to Li-ion batteries as efficient energy-storage devices for application in electric vehicles and energy storage systems owing to their low cost and resource abundance [1–5]. Transition metal dichalcogenides (TMDs), which take the form $MY_2$ (where M=Fe, Sn, Co, or Mo, and Y=S or Se) have been studied for application as anode materials in NIBs because they exhibit higher initial electrochemical decomposition plateau values compared to those of transition metal oxides [6–10]. Among the TMDs, $FeSe_2$, which is resource abundant, chemically stable, and non-toxic, has been reported as an anode material for NIBs [11–18]. Zhang et al. prepared $FeSe_2$ microspheres for the first time by a hydrothermal method and applied them as an anode material. This material delivered a discharge

* Corresponding authors.
*E-mail addresses:* yckang@korea.ac.kr (Y.C. Kang), jscho@cbnu.ac.kr (J.S. Cho).

https://doi.org/10.1016/j.cej.2018.01.118
Received 3 November 2017; Received in revised form 22 January 2018; Accepted 22 January 2018

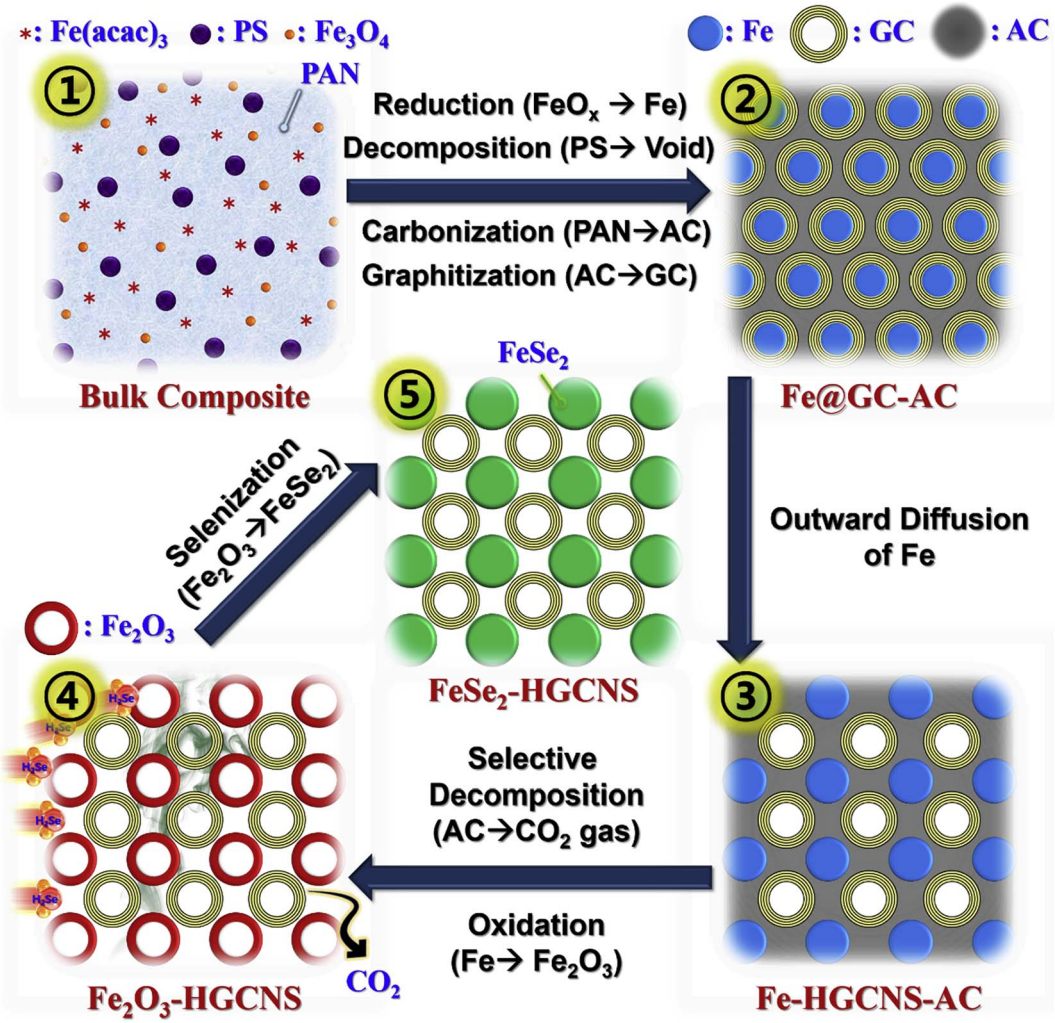


**Scheme 1.** Formation mechanism of $FeSe_2$-HGCNS composite by three sequential heat treatment steps and a subsequent selenization process.

capacity of 372 mA h $g^{-1}$ with a capacity retention of 89.0% after 2000 cycles at 1.0 A $g^{-1}$ [11]. Furthermore, Cho et al. synthesized nanofibers comprising reduced graphene oxide decorated with graphitic-carbon (GC)-coated hollow $FeSe_2$ nanospheres. The product delivered a discharge capacity of 412 mA h $g^{-1}$ after 150 cycles at 1.0 A $g^{-1}$ [12]. Moreover, Park et al. used a two-step method involving a spray drying process to synthesize $FeSe_2$-amorphous carbon composite powders. The discharge capacity of the powders for the 150th cycle at 0.5 A $g^{-1}$ was 379 mA h $g^{-1}$ [13].

Recently, porous GC materials have received increasing research attention as they can act as reservoirs for $Na^+$-ion storage and have channels for facile electrolyte permeation along with high electrical conductivity [19–24]. Therefore, the development of a highly efficient and cost-effective processes for the scalable production of TMD-combined porous GC structures is desired [22–24].

In this study, a simple and easily scalable process for the fabrication of $FeSe_2$ composited with hollow GC nanospheres (HGCNS) is introduced. The preparation of $FeSe_2$-HGCNS composite is performed by heating iron acetylacetonate, polystyrene, and polyacrylonitrile in a quartz beaker using a static furnace, followed by a subsequent simple selenization process. Unlike the general case where the polymers totally decompose into amorphous carbon (AC), the AC around the Fe is transformed into GC owing to the catalytic effect of the Fe. Initially, Fe metal crystals grow, and then the iron diffuses outward as the temperature increases, resulting in HGCNS. The highly conductive HGCNS are effective as a support material for active $FeSe_2$ nanocrystals because they can accommodate the strain arising from the volumetric changes of the $FeSe_2$ during sodiation/desodiation cycles. Furthermore, HGCNS that are well dispersed throughout the structure provide a three-dimensional (3D) network for the fast transfer of $Na^+$ ions and electrons so that very good rate capabilities can be achieved. Moreover, the porous GC matrix allows for the storage of $Na^+$ ions and easy penetration of the electrolyte. These synergetic effects result in excellent electrochemical properties, making $FeSe_2$-HGCNS composite a highly promising anode material for NIBs.

## 2. Experimental

### 2.1. Sample preparation

$FeSe_2$-hollow GC nanospheres (HGCNS) composite was synthesized using a quartz beaker placed in a static furnace with a subsequent simple selenization process. The precursor solution was prepared in the quartz beaker by dissolving 5 g of $Fe(acac)_3$, 5 g of polyacrylonitrile (PAN, $M_w$: 150,000), and 5 g of polystyrene (PS, $M_w$: 192,000) in 100 mL of *N,N*-dimethylformamide (DMF) with vigorous stirring overnight. The quartz beaker containing the solution was then transferred to a static furnace and subjected to a three-step post-treatment process. First, the solution was dried for 1 h at 150 °C in air to evaporate the solvent. Then, the dried solution was carbonized at 700 °C for 3 h at a heating rate of 5 °C $min^{-1}$ under a 10% $H_2$/Ar gas mixture. Finally, the powders were treated at 300 °C for 3 h at a heating rate of 5 °C $min^{-1}$ in

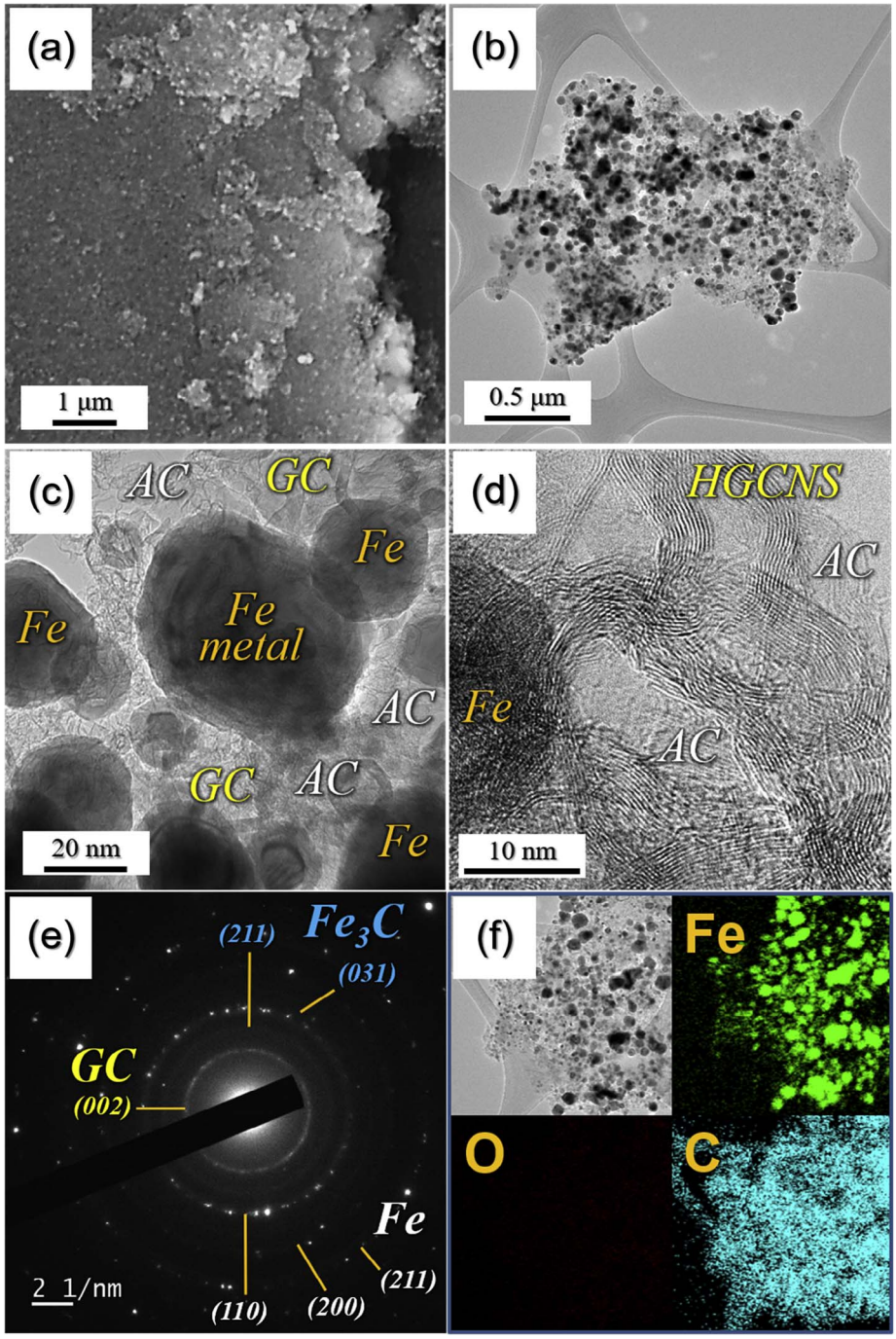


**Fig. 1.** Morphologies, SAED pattern, and elemental mapping images of the sample obtained after reduction of second step at 700 °C: (a) FE-SEM image, (b) TEM image, (c, d) HR-TEM images, (e) SAED pattern, and (f) elemental mapping images.

air to decompose the amorphous carbon (AC). The resultant powder was then selenized at 300 °C for 10 h under 10% $H_2$/Ar using powdered Se. The selenization process is described in detail in our previous reports [25,26]. For the selenization process, the powders and selenium-metal powders were loaded in a covered alumina boat and placed in a quartz-tube reactor. The porous structure prepared from combustion of PS enabled good pathway for the reducing vapor fumigation. $H_2Se$ gas was formed from the reaction of the powdered Se with $H_2$ gas via the following reaction: Se (s) + $H_2$ (g) → $H_2Se$ (g). For comparison purposes, bare $FeSe_2$ powders, i.e., $FeSe_2$ powders that did not contain HGCNS, were also prepared. In these cases, dried powders were directly treated at 700 °C for 3 h in air (5 °C $min^{-1}$) without the carbonization step, and the powders were then selenized under 10% $H_2$/Ar atmosphere at 350 °C to obtain pure $FeSe_2$.

### 2.2. Characterization techniques

The microstructures of the materials were observed by field-emission scanning electron microscopy (FE-SEM, S-4800, Hitachi) and field-emission transmission electron microscopy (FE-TEM, JEM-2100F, JEOL). In addition, their crystal phases were evaluated by X-ray diffractometry (XRD, X'Pert PRO MPD) using Cu $K_\alpha$ radiation ($\lambda$ = 1.5418 Å). X-ray photoelectron spectroscopy (XPS, Thermo Scientific K-Alpha) using focused monochromatic Al $K_\alpha$ radiation at 12 kV and 20 mA was employed to analyze the compositions of the samples. The structure of the carbonaceous materials was characterized via Raman spectroscopy (Jobin Yvon LabRam, HR800, excitation source = 632.8 nm He–Ne laser) at room temperature. The surface areas of the powders were measured by the Brunauer-Emmett-Teller (BET) method using $N_2$ as the adsorbate gas. Thermogravimetric

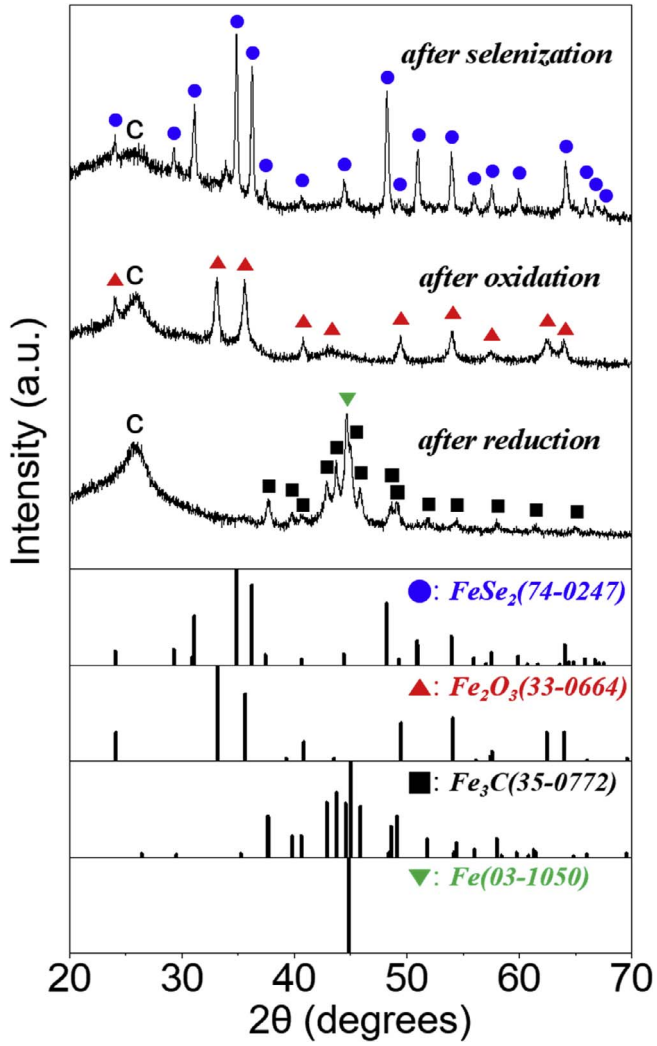


**Fig. 2.** XRD patterns of the samples obtained from a beaker after each step.

analysis was performed using a Pyris 1 TGA (Perkin Elmer) over a temperature range of 25–650 °C and at a heating rate of 10 °C $min^{-1}$ under a static air atmosphere.

### 2.3. Electrochemical measurements

The electrochemical properties of the materials were analyzed by constructing 2032-type coin cells. The anodes were prepared by mixing the active material, carbon black, and sodium carboxymethyl cellulose (CMC) at a weight ratio of 7:2:1. Na metal and microporous polypropylene films were used as the counter electrodes and the separators, respectively. The electrolyte was 1 M $NaClO_4$ with 5% fluoroethylene carbonate (FEC) dissolved in a mixture of ethylene carbonate/dimethyl carbonate (EC/DMC; 1:1 *v/v*). The discharge/charge characteristics of the samples were investigated by cycling over a 0.001–3.0 V potential range at various current densities. Cyclic voltammograms (CVs) were measured at a scan rate of 0.1 mV $s^{-1}$. The diameter of the negative electrode containing the $FeSe_2$ powder was 1.4 cm and the mass loading was approximately 1.2 mg $cm^{-2}$. Electrochemical impedance spectra were obtained by performing alternating-current electrochemical impedance spectroscopy (EIS, ZIVE SP1) over a frequency range of 0.01 Hz to 100 kHz.

## 3. Results and discussion

The formation mechanism for $FeSe_2$-hollow GC nanospheres (HGCNS) composite is shown in Scheme 1. During the first step, Fe(acac)$_3$-$Fe_3O_4$-PAN-PS composite is obtained upon drying the DMF solution in a beaker at 150 °C in air (Scheme 1-①). In the early stage of the second step, both Fe(acac)$_3$ and $Fe_3O_4$ are reduced to metallic Fe and PAN is concurrently carbonized to AC at 700 °C under 10% $H_2$/Ar atmosphere. Then, under the influence of the Fe metal acting as a catalyst, the AC surrounding the metallic Fe nanoparticles is transformed into GC (Scheme 1-②) [27,28]. The activation energy of the AC-to-GC transformation is lowered owing to the catalyst, thus graphitization occurs under the relatively low temperature of 700 °C. Additionally, the voids formed by the complete decomposition of the PS provide pathways in the AC matrix for facile penetration of the reducing gas. Therefore, the metallic Fe nanoparticles nucleate and then form core–shell-structured Fe@GC nanospheres (Scheme 1-②). Subsequently, the Fe in the cores diffuses outward by an Ostwald ripening process, forming Fe nanoparticles well-distributed within the AC and HGCNS matrix during the second step (Scheme 1-③). In the third step, AC materials are selectively decomposed into $CO_2$ gas under air and the solid Fe metal surrounded by HGCNS is transformed into $Fe_2O_3$ (Scheme 1-④). Finally, the $Fe_2O_3$ is selenized to $FeSe_2$ during the selenization process (Scheme 1-⑤). In summary, a DMF solution containing Fe(acac)$_3$, PAN, and PS is transformed into a nanocrystalline $FeSe_2$-HGCNS composite by a static three-step post-treatment and subsequent selenization.

The formation mechanism of $FeSe_2$-HGCNS composite was investigated based on the morphologies and crystal structures of samples obtained following each step. The SEM image and XRD pattern of the bulk composite obtained after the first drying step at 150 °C is shown in Fig. S1. The XRD pattern of the dried sample reveals small peaks for the $Fe_3O_4$ phase formed by the partial decomposition of Fe(acac)$_3$. Since the decomposition temperatures of PAN and PS are approximately 240 and 320 °C, respectively, the bulk sample formed in the drying step is an Fe(acac)$_3$-$Fe_3O_4$-PAN-PS composite. The dried sample obtained after the first step is reduced at 700 °C in the second step by changing the gas. The SEM and low-resolution TEM images shown in Fig. 1a and b, respectively, show the porous structure of the bulk composite obtained after the reduction process. The PS and PAN in the composite are decomposed into $CO_2$ gas and carbonized to AC, respectively, to form a porous carbon structure in which the pores act as a 3D network of channels for the facile penetration of the reducing gas. Therefore, nanosized Fe metal particles are formed and distributed uniformly throughout the AC matrix, as confirmed in Fig. 2. Notably, onion-like GC layers are initially formed surrounding the Fe metal nanospheres at the relatively low temperature of 500 °C by Fe catalysis, as shown in Fig. S2. However, as the reduction temperature is increased to 700 °C, the core Fe metal diffuses out of the shells by Ostwald ripening process, as described in Scheme 1-②-③. In this step, ultrafine Fe nanocrystals form and coalesce, resulting in HGCNS. Therefore, Fe metal nanoparticles surrounded by both HGCNS and the AC matrix are observed in the TEM images in Fig. 1c and d. In order to verify the catalytic activity of iron, we have prepared DMF solution (100 mL DMF containing 5 g PS and 5 g PAN) without iron salt. The dried solution was subjected to reduction at 700 °C for 3 h and its TEM images were obtained and shown in Fig. S3a and b. Amorphous carbon was observed as shown in the HR-TEM image (Fig. S3b), which is in good agreement with the SAED pattern in Fig. S3c. In the XRD pattern shown in Fig. 2, peaks for $Fe_3C$ are also observed. This is because $Fe_3C$ forms on the parts of the Fe metal surfaces in contact with carbon [29]. The selected area electron diffraction (SAED) pattern shown in Fig. 1e reveals a mixed crystalline structure comprising Fe, carbon, and $Fe_3C$ phases. The elemental mapping images shown in Fig. 1f show a trace amount of oxygen and reveal the formation of a carbon matrix with a uniform distribution of Fe nanoparticles. The trace amount of oxygen could be owing to the surface oxidation of iron metal, with high reactivity, exposed to air atmosphere before the analysis.

During the third step, performed at 300 °C under air, the AC

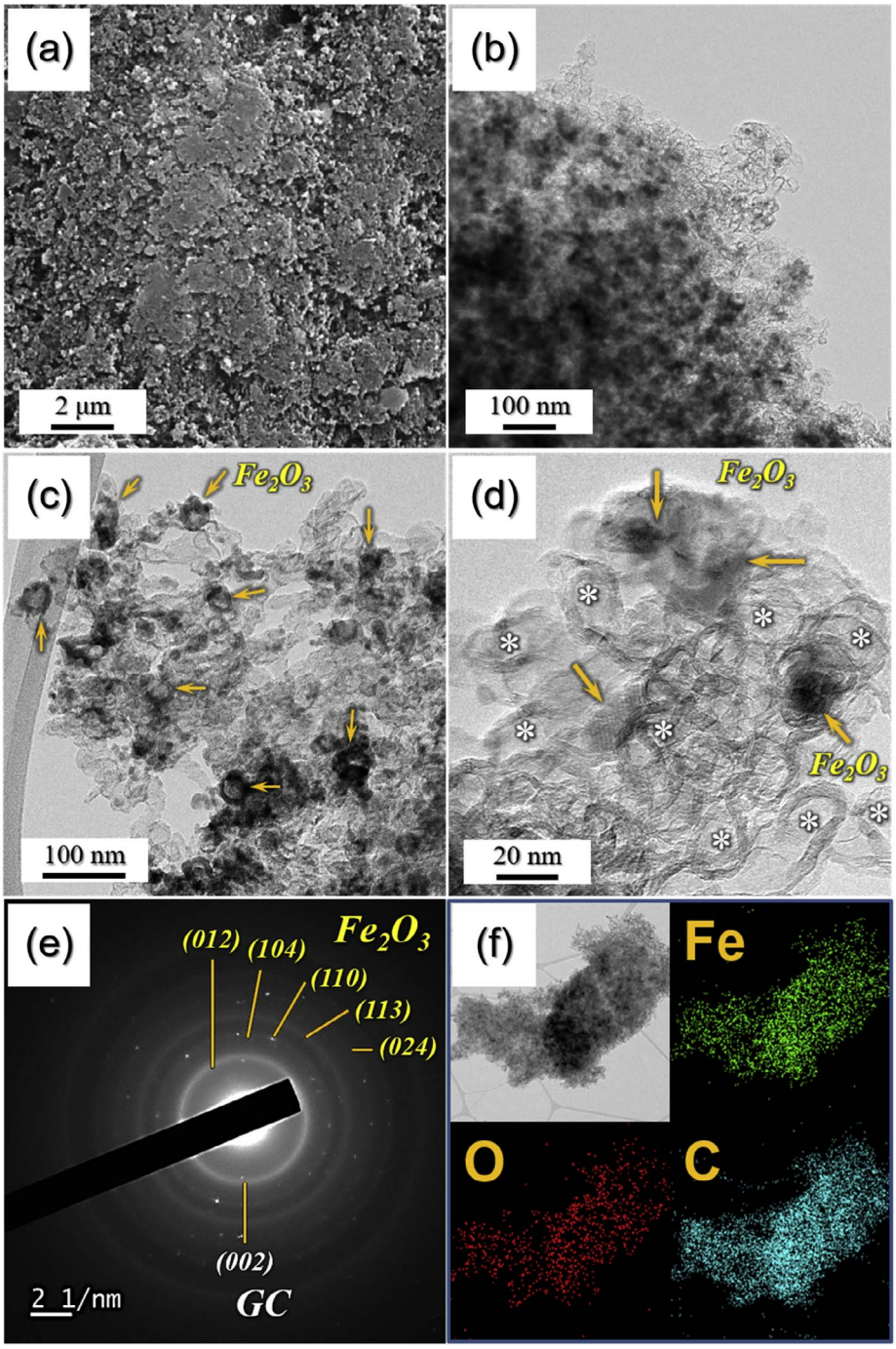


**Fig. 3.** Morphologies, SAED pattern, and elemental mapping images of the sample obtained after oxidation of the third step at 300 °C: (a) FE-SEM image, (b, c) TEM images, (d) HR-TEM image, (e) SAED pattern, and (f) elemental mapping images.

material in the composite is selectively removed. The morphology of the sample obtained after the third step is shown in Fig. 3. Fe metal and additional $Fe_3C$ phases are completely transformed into a monophase of cubic $Fe_2O_3$ during the oxidation, as shown in Fig. 2. Well-dispersed hollow $Fe_2O_3$ nanoparticles formed by Kirkendall diffusion surrounded by HGCNS can be observed in the SEM and low-resolution TEM images presented in Fig. 3a–d. Selective removal of the AC component, leaving $Fe_2O_3$ nanoparticles (as indicated by arrows) and HGCNS (marked with asterisks) is confirmed by the TEM images in Fig. 3c and d. The asterisks in Fig. 3d indicate where the Fe metal was once located before it diffused outward during the reduction process. The SAED patterns in Fig. 3e further confirm the formation of the $Fe_2O_3$ phase, which is also supported by the elemental mapping images in Fig. 3f that show the existence of well-dispersed $Fe_2O_3$ nanoparticles. $Fe_2O_3$ and elemental carbon are also observed throughout the sample, indicating that $Fe_2O_3$ is uniformly distributed in HGCNS matrix. The selective removal of AC is further confirmed by comparing the Raman analyses of the samples before and after the third step, as shown in Fig. 4. The resonances at 1360 and 1590 $cm^{-1}$ in the Raman spectra can be assigned to the D and G bands of carbon, respectively, with the G-band characteristic of graphite [30,31]. The degree of graphitization of a carbon material can typically be evaluated according to the ratio of the intensity of the D-band ($I_D$) to that of the G-band ($I_G$) [30,31]. The peak intensity ratio $I_D/I_G$ decreases from 1.35 before the third step to 0.81 after the step, indicating that the disordered AC material in the composite is selectively removed at 300 °C during the third step.

In order to transform the $Fe_2O_3$ into $FeSe_2$, the sample obtained after the third step was selenized at 300 °C under 10% $H_2$/Ar. The

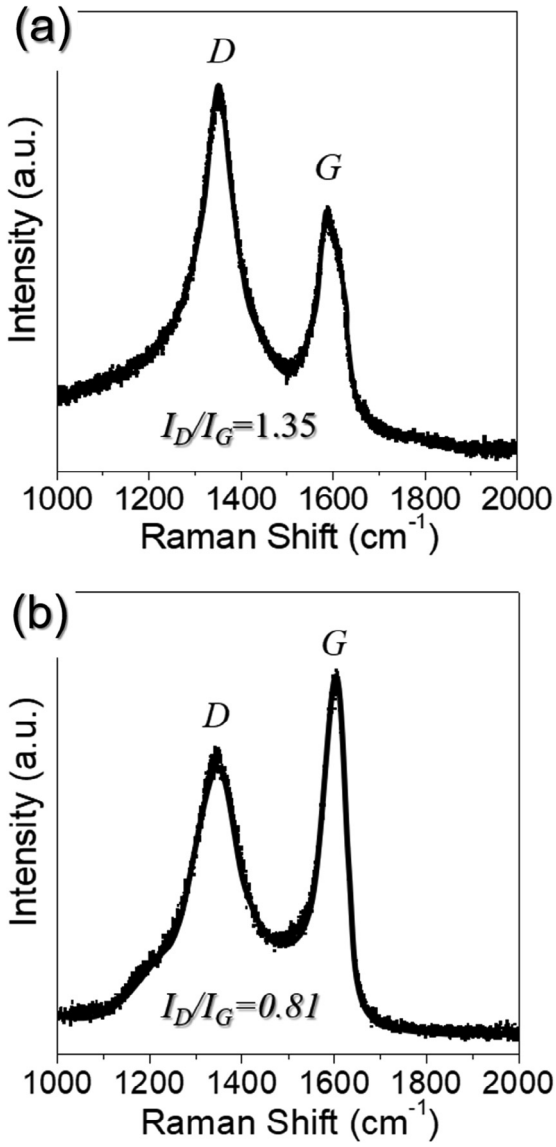


**Fig. 4.** Raman spectra of the samples (a) before and (b) after the oxidation of the third step for selectively decomposition of AC.

morphology of $FeSe_2$-HGCNS composite obtained after the selenization is shown in Fig. 5. $Fe_2O_3$ nanoparticles surrounded by HGCNS are successfully transformed into $FeSe_2$ during the process, as confirmed by the phase analysis in Fig. 2. The original hollow $Fe_2O_3$ nanoparticles transformed into solid $FeSe_2$ nanoparticles by sintering process during selenization [32,33]. Fig. 5a–c show $FeSe_2$ nanoparticles (as indicated by arrows in Fig. 5c) randomly distributed within clearly distinguishable HGCNS. The yellow dotted and green solid lines shown in the HR-TEM image in Fig. 5d indicate the boundaries of the $FeSe_2$ nanoparticles and HGCNS, respectively. In the HR-TEM image in Fig. 5e, clear void spaces in GC shells with clear lattice fringes separated by 0.34 nm, which correspond to the (0 0 2) crystal planes of the GC phase, can be observed. The thicknesses of the GC shells are ~8–10 nm. $FeSe_2$ nanoparticles showing clear lattice fringes with d-spacings of 0.26 nm, attributed to the (1 1 1) lattice planes of orthorhombic $FeSe_2$, are observed in Fig. 5f. The SAED patterns in the inset image of Fig. 5f further confirm the existence of the $FeSe_2$ and GC. In the elemental mapping images shown in Fig. 5g, $FeSe_2$ particles can be explicitly distinguished from the carbon component.

To elucidate the chemical nature of $FeSe_2$-HGCNS composite, it was characterized using XPS, as shown in Fig. 6. The XPS survey scan shown in Fig. 6a reveals distinct peaks indicating the presence of Fe, C, and Se. In Fig. 6b, distinct Fe $2p_{3/2}$ and Fe $2p_{1/2}$ doublets for both $FeSe_2$ and iron oxides can be observed. The peaks located at 706.7 and 719.3 eV correspond to Fe $2p_{3/2}$ and Fe $2p_{1/2}$, respectively, revealing the existence of $Fe^{2+}$ in $FeSe_2$. [13,34,35]. Furthermore, peaks located at 709.8/711.1 eV and 724/726.1 eV correspond to Fe $2p_{3/2}$ and Fe $2p_{1/2}$ for the $Fe^{2+}/Fe^{3+}$ in the iron oxides, respectively [36,37]. The high reactivity of $FeSe_2$ with oxygen causes its partial oxidation into iron oxides [13,34]. The Se 3d spectrum shown in Fig. 6c shows a large-intensity peak that can be deconvoluted into peaks at 54.2 and 55.0 eV, representing Se $3d_{5/2}$ and Se $3d_{3/2}$, respectively; which are characteristic peaks of $FeSe_2$ [13,34,35]. The peak observed at 58.6 eV is related to Se-O bonding [12,38]. The Se-O bond signal confirms the existence of a small amount of $SeO_2$ impurities formed by the partial oxidation of $FeSe_2$ [12,18]. The C 1s spectrum shown in Fig. 6d reveals the presence of carbon in a variety of bonding states, with O—C=O, C=O, C—O, $sp^3$ C—C, and $sp^2$ C—C bonding peaks at 288.3, 287.5, 286.1, 284.8, and 284 eV, respectively [39–41]. The $sp^2$ C—C bonding presents the highest-intensity peak, indicating that GC is the major component of $FeSe_2$-HGCNS composite, which is in good agreement with the structure evolution process proposed above [41]. The results of thermogravimetric (TG) analysis for $FeSe_2$-HGCNS composite are presented in Fig. 7. A one-step weight gain and multiple-step weight losses are observed below 600 °C. The slight weight increase near 230 °C is due to the partial oxidation of $FeSe_2$ resulting in the formation of an $FeSeO_x$ phase. Weight decreases are observed between 250 and 600 °C owing to both the conversion of $FeSeO_x$ and $FeSe_2$ to $Fe_2O_3$ and the combustion of HGCNS. A GC content of 25% was calculated from the TG curve of $FeSe_2$-HGCNS composite.

Bare $FeSe_2$ powder without HGCNS for comparison purposes is prepared and shown in Fig. S4c and d. Bare intermediate $Fe_2O_3$ powder characterized in Fig. S4a and b was prepared by directly post-treating the sample obtained after the first drying step at 700 °C under air. The selenization of the bare $Fe_2O_3$ powder at 350 °C produces rod-shaped pure $FeSe_2$ particles, as identified in Fig. S4c and d. The XRD patterns shown in Fig. S4b and d confirm the complete conversion of $Fe_2O_3$ to $FeSe_2$ during the selenization process. The BET surface areas of $FeSe_2$-HGCNS composite and bare $FeSe_2$ powder are 88.4, and 3.8 $m^2 g^{-1}$, respectively, as shown in Fig. S5. The well-developed mesopores provided by HGCNS result in the much higher BET surface area of $FeSe_2$-HGCNS composite. The H3 hysteresis loop of the type IV isotherm and Barrett-Joyner-Halenda (BJH) pore size distributions for $FeSe_2$-HGCNS composite indicate the presence of a substantial amount of mesopores with a mean diameter of 3 nm that can act as reservoirs for $Na^+$-ion storage and as channels for easy permeation of the electrolyte during repeated sodiation/desodiation cycles.

The electrochemical properties of $FeSe_2$-HGCNS composite as an anode material for NIBs are compared with those of bare $FeSe_2$ in Fig. 8. The CV curves of $FeSe_2$-HGCNS composite for the first five cycles are shown in Fig. 8a. The following equations clearly describe the electrochemical reactions that occur during discharge/charged processes.

Discharge process equations:

$$FeSe_2 + xNa^+ + xe^- \rightarrow Na_xFeSe_2 \quad (1)$$

$$Na_xFeSe_2 + (2-x)Na^+ + (2-x)e^- \rightarrow Na_2Se + FeSe \quad (2)$$

$$FeSe + 2Na^+ + 2e^- \rightarrow Fe + Na_2Se \quad (3)$$

Charge process equations:

$$Fe + Na_2Se \rightarrow FeSe + 2Na^+ + 2e^- \quad (4)$$

$$FeSe + Na_2Se \rightarrow Na_xFeSe_2 + (2-x)Na^+ + (2-x)e^- \quad (5)$$

$$Na_xFeSe_2 \rightarrow FeSe_2 + xNa^+ + xe^- \quad (6)$$

Five distinguishable peaks at 2.0, 1.8, 1.1, 0.6, and 0.4 V are observed during the first cathodic scan. The peaks at 1.8 and 2.0 V may be

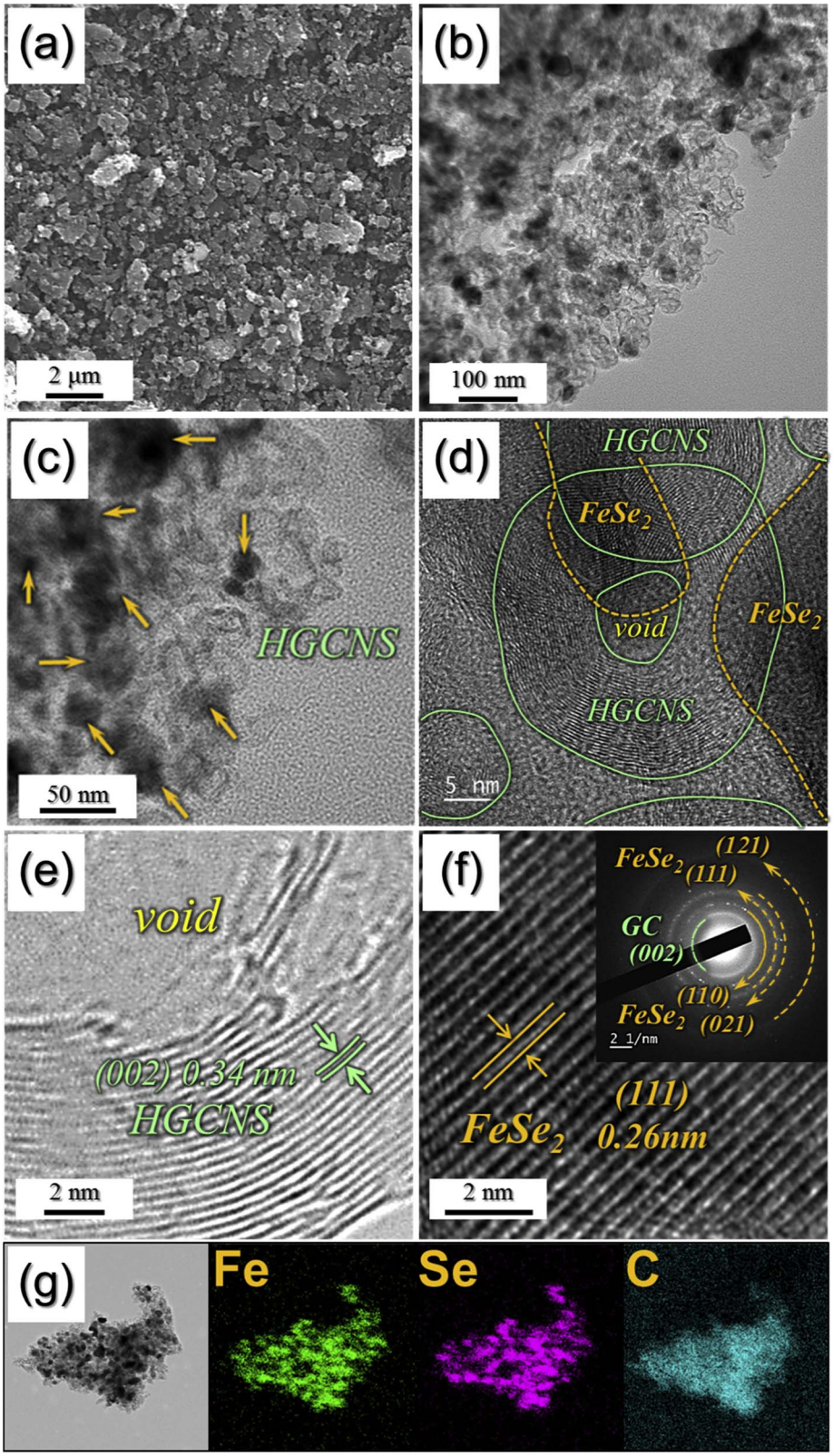


**Fig. 5.** Morphologies, SAED pattern, and elemental mapping images of $FeSe_2$-HGCNS composite obtained after selenization at 300 °C: (a) FE-SEM image, (b, c) TEM images, (d, e) HR-TEM images, (f) HR lattice image and SAED pattern, and (g) elemental mapping images.

attributed to the electrochemical reactions between metalloid selenium and sodium ions, which disappeared from the 2nd cycle and on [25,42,43]. The peak at 1.1 V corresponds to the formation of both $Na_xFeSe_2$ and a solid electrolyte interphase (SEI) by electrolyte decomposition corresponding to Eq. (1) [11–13]. The two peaks at 0.6 and 0.4 V are attributed to the formation of FeSe and $Na_2Se$ (2), and Fe and $Na_2Se$ (3), respectively [11–13]. Four oxidation peaks located at 1.5, 1.9, 2.1, and 2.4 V are observed in the first anodic scan. The peaks at 1.5 and 1.9 V are attributed to the formation of FeSe (4) and $Na_xFeSe_2$ (5), respectively, whereas the peak at 2.1 is derived from the formation of $FeSe_2$ (6) [11–13]. Another peak at 2.4 V corresponds to the decomposition of SEI layer. From the second cycle and on, SEI layer was

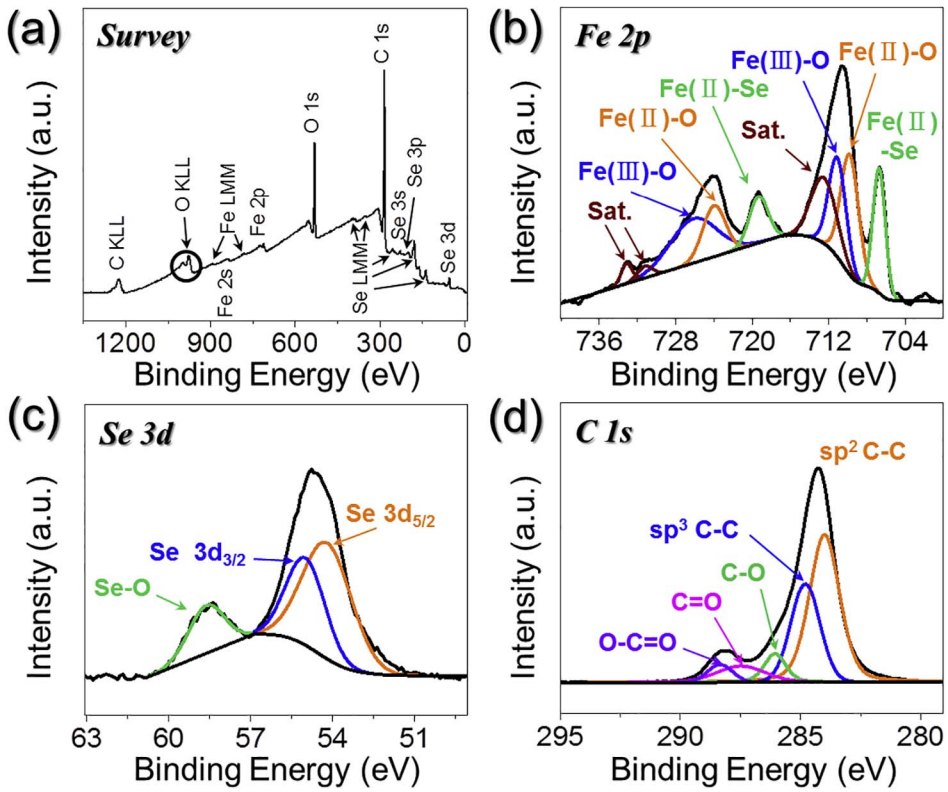


**Fig. 6.** XPS spectra of $FeSe_2$-HGCNS composite obtained after selenization process: (a) survey, (b) Fe 2p, (c) Se 3d, and (d) C 1s.

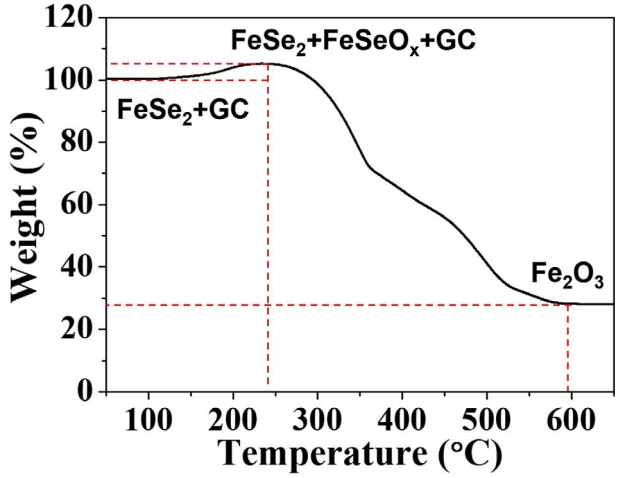


**Fig. 7.** TG curve of $FeSe_2$-HGCNS composite obtained after selenization process.

partially composed and decomposed during discharging and charging processes at 1.8 and 2.4 V, respectively [44–47]. Overall, the CV curve for $FeSe_2$-HGCNS composite shown in Fig. 8a is similar to those of $FeSe_2$-carbon composite materials presented previously in the literatures [11–13]. From the second cycle onward, the reduction peaks shift to higher potentials owing to the formation of ultrafine $FeSe_2$ nanocrystals during the first charge/discharge processes [12,48]. The shapes of the CV curves from the second cycle onwards are almost identical, demonstrating the excellent electrochemical stability of $FeSe_2$-HGCNS composite. The CV curves of bare $FeSe_2$ showed almost similar peaks as $FeSe_2$-HGCNS composite material as shown in Fig. S6. Fig. 8b shows the discharge/charge profile curves of both $FeSe_2$ materials in the potential range 0.001–3.0 V at a current density of 0.5 A $g^{-1}$. Plateaus at 1.8 and 1.1 V were attributed to electrochemical reactions between remaining selenium and sodium ion, and formation of $Na_xFeSe_2$ and SEI layer by electrolyte decomposition, respectively, coincide well for the two samples [11–13,25,42,43]. Also, the presence of four oxidation peaks at 1.5, 1.9, 2.1, and 2.4 V further verified the coincidence.

The cycling performances of $FeSe_2$-HGCNS composite and bare $FeSe_2$ at a current density of 0.5 A $g^{-1}$ are shown in Fig. 8c. $FeSe_2$-HGCNS composite and bare $FeSe_2$ deliver initial capacities of 670 and 516 mA h $g^{-1}$, respectively, and their corresponding coulombic efficiencies are 68 and 87%, respectively. The amount of active material in $FeSe_2$-HGCNS composite is less than that in bare sample in a unit. Therefore, bare sample's initial reversible specific capacity should be higher than that of the composite. However, the polarization caused by slow sodium-ion diffusion resulted in the low initial reversible specific capacity of bare $FeSe_2$. The initial charge/discharge profile of bare $FeSe_2$ powders at a current density of 0.05 A $g^{-1}$ is shown in Fig. S7. The low initial Coulombic efficiency of $FeSe_2$-HGCNS composite is attributed to the high initial capacity loss of the carbon component [8,49]. The discharge capacities of $FeSe_2$-HGCNS composite and bare $FeSe_2$ powder after 100 cycles at the high current density of 0.5 A $g^{-1}$ are 425 and 115 mA h $g^{-1}$, respectively. $FeSe_2$-HGCNS composite exhibits superior cycling behavior because it contains smaller $FeSe_2$ particles surrounded by HGCNS. HGCNS without $FeSe_2$ was prepared by selectively etching $FeSe_2$ in $FeSe_2$-HGCNS composite with nitric acid (60%) and then cycle test was conducted to acknowledge the capacity of contribution of HGCNS in $FeSe_2$-HGCNS composite powders. The initial charge/discharge profile and cycling performance of HGCNS at a current density of 0.5 A $g^{-1}$ are shown in the Fig. S8a and b, respectively. Based on the capacity of HGCNS and the carbon content (25 wt %), the capacity of $FeSe_2$ material alone was calculated and its cycle performance is shown in Fig. S8c. The second discharge capacity of $FeSe_2$ material was 495 mA h $g^{-1}$, which is similar to that of the theoretical capacity of $FeSe_2$. $FeSe_2$-HGCNS composite maintained its morphology well after cycling as shown in Fig. S9a; ultrafine $FeSe_2$ nanocrystals around the hollow graphitic carbon rings could be well observed after 80 cycles. On the other hand, fractured $FeSe_2$ particles were observed for bare $FeSe_2$ electrode after cycling. The excellent $Na^+$-ion storage behavior of $FeSe_2$-HGCNS composite is demonstrated

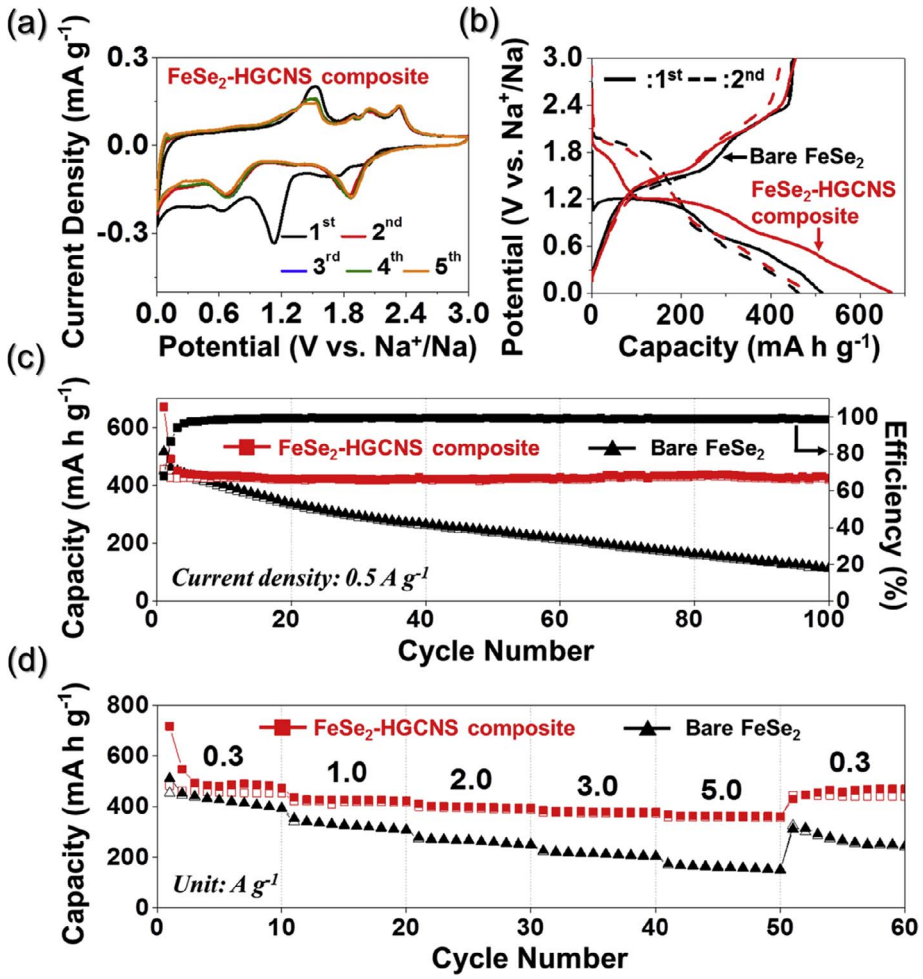


**Fig. 8.** Electrochemical properties of $FeSe_2$-HGCNS composite and bare $FeSe_2$: (a) CV curves of $FeSe_2$-HGCNS, (b) 1st and 2nd discharge–charge curves at a current density of 0.5 A $g^{-1}$, (c) cycling performances, and (d) rate performances of $FeSe_2$-HGCNS.

by its rate performance, shown in Fig. 8d. At current densities of 0.3, 1.0, 2.0, 3.0, and 5.0 A $g^{-1}$, the discharge capacities of $FeSe_2$-HGCNS composite are 472, 422, 393, 378, and 361 mA h $g^{-1}$, respectively. It is noteworthy that, after cycling at high current densities, when the current density returns to 0.3 A $g^{-1}$, the discharge capacity recovers well to 469 mA h $g^{-1}$ and the sample continues to exhibit stable cyclability. On the other hand, bare $FeSe_2$ with low ionic conductivity showed inferior rate performance. The discharge capacities of bare $FeSe_2$ powders at current densities of 0.3, 1.0, 2.0, 3.0, and 5.0 A $g^{-1}$ were 393, 309, 251, 205, and 151 mA h $g^{-1}$, respectively. This structure is beneficial for the conversion reaction in way that high conductivity HGCNS that are well-dispersed throughout the structures develop a 3D channel network for $Na^+$ ions and electrons. In addition, ultrafine $FeSe_2$ surrounded by HGCNS provide high $Na^+$ ion diffusivity. Due to its synergetic structural merits, high reversibility is achieved and the anode material exhibited excellent rate capability. $FeSe_2$-HGCNS composite showed superior electrochemical performances compared to those of other $FeSe_2$ materials reported in the previous literatures as summarized in Table S1.

EIS analysis of the samples was performed before and after 100 cycles to investigate the superior $Na^+$-ion storage properties of $FeSe_2$-HGCNS composite. The Nyquist plots deconvoluted with a Randle-type equivalent-circuit model for $FeSe_2$-HGCNS composite and the bare $FeSe_2$ powder are presented in Fig. 9. The semicircles in the medium-frequency region correspond to the charge transfer resistance ($R_{ct}$) of the electrodes [50–53]. The $R_{ct}$ values for $FeSe_2$-HGCNS composite and bare $FeSe_2$ are 231 and 306 Ω, respectively. Thus, $FeSe_2$ electrode containing high-electrical-conductivity GC exhibits a lower $R_{ct}$ value than that of bare $FeSe_2$. The $R_{ct}$ values of $FeSe_2$-HGCNS composite and bare $FeSe_2$ after the 100th cycle are 91 and 166 Ω, respectively. The much higher $R_{ct}$ value for the bare $FeSe_2$ powder is due to structural disintegration of the sample over 100 cycles. However, the $R_{ct}$ value of $FeSe_2$-HGCNS composite remains low, even after 100 cycles. This is because HGCNS effectively support the active $FeSe_2$ nanocrystals and accommodate the volume change of $FeSe_2$ during repeated sodiation/desodiation cycles. Additionally, fast electrons and $Na^+$-ion transfer occurs through the porous 3D network formed by the highly conductive HGCNS and ultrafine $FeSe_2$ nanocrystals. In order to clearly show the effect of graphitic carbon, we assembled coin cell that does not contain super P material for both $FeSe_2$-HGCNS composite and bare $FeSe_2$. The Nyquist plots of the samples before cycling are shown in Fig. S10. The $R_{ct}$ values of $FeSe_2$-HGCNS composite with super P and without super P were 231 and 370 Ω, respectively, whereas those of bare $FeSe_2$ were 306 and 581 Ω, respectively. $FeSe_2$ composited with HGCNS exhibited much lower $R_{ct}$ value than bare $FeSe_2$ when the cell was assembled without super P. 20% carbon black was added for synergetic effects of HGCNS with super P material to obtain better electrochemical performance. These EIS results confirm the effect of HGCNS on the structural stability of $FeSe_2$-HGCNS composite. In summary, the high structural stability and fast $Na^+$-ion and electron transfer of $FeSe_2$-HGCNS composite provides it with superior $Na^+$-ion storage properties.

## 4. Conclusions

A scalable process for the synthesis of $FeSe_2$-HGCNS composite is presented. A solution containing the metal salt and organic polymers was easily prepared in a quartz beaker and transformed into the final product by three sequential heat treatment steps and a subsequent

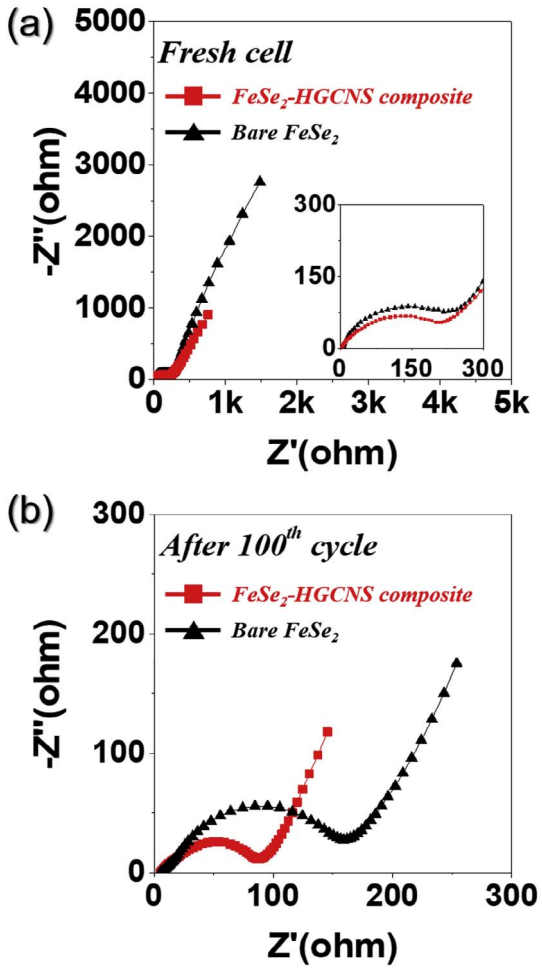


**Fig. 9.** Nyquist impedance plots of $FeSe_2$-HGCNS composite and bare $FeSe_2$: (a) before cycling, and (b) after 100th cycles.

selenization process. PS decomposition provides pathways for the reducing gas, resulting in Fe nanoparticles uniformly embedded in an AC matrix containing HGCNS. The oxidation step selectively removes the AC component and leads to the simultaneous formation of $Fe_2O_3$ nanoparticles. After the final selenization process, $FeSe_2$ nanoparticles surrounded by HGCNS are obtained. The composite exhibits excellent $Na^+$-ion storage performance due to ultrafine $FeSe_2$ nanocrystals and HGCNS, which provide high sodium ion diffusivity in the structure, accommodate the volume changes of the $FeSe_2$, and provide high electronic conductivity. Moreover, the porous 3D network composed of highly conductive HGCNS allows fast transfer of electrons and easy penetration of the electrolyte during cycling. The simple strategy introduced here can be widely applied in the large-scale synthesis of metal chalcogenide particle-GC composites for various applications including energy storage.

## Acknowledgements

This research was supported by the Technology Development Program to Solve Climate Changes of the National Research Foundation (NRF) funded by the Ministry of Science, ICT & Future Planning (2017M1A2A2087577). This work was supported by the National Research Foundation of Korea (NRF) Grant funded by the Korea government (MSIP) (No. 2017R1A2B2008592).

## Appendix A. Supplementary data

Supplementary data associated with this article can be found, in the online version, at http://dx.doi.org/10.1016/j.cej.2018.01.118.

## References

[1] M.D. Slater, D. Kim, E. Lee, C.S. Johnson, Sodium-ion batteries, Adv. Funct. Mater. 23 (2013) 947–958.
[2] S.W. Kim, D.H. Seo, X. Ma, G. Ceder, K. Kang, Electrode materials for rechargeable sodium-ion batteries: potential alternatives to current lithium-ion batteries, Adv. Energy Mater. 2 (2012) 710–721.
[3] N. Yabuuchi, K. Kubota, M. Dahbi, S. Komaba, Research development on sodium-ion batteries, Chem. Rev. 114 (2014) 11636–11682.
[4] L. Si, Z. Yuan, L. Hu, Y. Zhu, Y. Qian, Uniform and continuous carbon coated sodium vanadium phosphate cathode materials for sodium-ion battery, J. Power Sources 272 (2014) 880–885.
[5] Z. Yuan, L. Si, X. Zhu, Three-dimensional hard carbon matrix for sodium-ion battery anode with superior-rate performance and ultralong cycle life, J. Mater. Chem. A 3 (2015) 23403–23411.
[6] C. Wu, Y. Jiang, P. Kopold, P.A. van Aken, J. Maier, Y. Yu, Peapod-like carbon-encapsulated cobalt chalcogenide nanowires as cycle-stable and high-rate materials for sodium-ion anodes, Adv. Mater. 28 (2016) 7276–7283.
[7] J.S. Park, Y.C. Kang, Multicomponent (Mo, Ni) metal sulfide and selenide microspheres with empty nanovoids as anode materials for Na-ion batteries, J. Mater. Chem. A 5 (2017) 8616–8623.
[8] G. Li, D. Luo, X. Wang, M.H. Seo, S. Hemmati, A. Yu, Z. Chen, Enhanced reversible sodium-ion intercalation by synergistic coupling of few-layered MoS2 and S-doped graphene, Adv. Funct. Mater. 27 (2017) 1702562.
[9] C. Zhu, P. Kopold, W. Li, P.A. van Aken, J. Maier, Y. Yu, Engineering nanostructured electrode materials for high performance sodium ion batteries: a case study of a 3D porous interconnected $WS_2$/C nanocomposite, J. Mater. Chem. A 3 (2015) 20487–20493.
[10] L. Zhou, K. Zhang, J. Sheng, Q. An, Z. Tao, Y.M. Kang, J. Chen, L. Mai, Structural and chemical synergistic effect of CoS nanoparticles and porous carbon nanorods for high-performance sodium storage, Nano Energy 35 (2017) 281–289.
[11] K. Zhang, Z. Hu, X. Liu, Z. Tao, J. Chen, $FeSe_2$ microspheres as a high-performance anode material for Na-ion batteries, Adv. Mater. 27 (2015) 3305–3309.
[12] J.S. Cho, J.K. Lee, Y.C. Kang, Graphitic carbon-coated $FeSe_2$ hollow nanosphere-decorated reduced graphene oxide hybrid nanofibers as an efficient anode material for sodium ion batteries, Sci. Rep. 6 (2016) 23699.
[13] G.D. Park, J.H. Kim, Y.C. Kang, Large-scale production of spherical $FeSe_2$-amorphous carbon composite powders as anode materials for sodium-ion batteries, Mater. Charact. 120 (2016) 349–356.
[14] X. Wei, C. Tang, Q. An, M. Yan, X. Wang, P. Hu, X. Cai, L. Mai, $FeSe_2$ clusters with excellent cyclability and rate capability for sodium-ion batteries, Nano Res. 10 (2017) 3202–3211.
[15] W. Zhao, C. Guo, C.M. Li, Lychee-like $FeS_2$@$FeSe_2$ core–shell microspheres anode in sodium ion batteries for large capacity and ultralong cycle life, J. Mater. Chem. A 5 (2017) 19195–19202.
[16] Z. Zhang, X. Shi, X. Yang, Y. Fu, K. Zhang, Y. Lai, J. Li, Nanooctahedra particles assembled $FeSe_2$ microspheres embedded into sulfur-doped reduced graphene oxide sheets as a promising anode for sodium ion batteries, ACS Appl. Mater. Interfaces 8 (2016) 13849–13856.
[17] F. Zhao, S. Shen, L. Cheng, L. Ma, J. Zhou, H. Ye, N. Han, T. Wu, Y. Li, J. Lu, Improved sodium-ion storage performance of ultrasmall iron selenide nanoparticles, Nano Lett. 17 (2017) 4137–4142.
[18] H. Fan, H. Yu, Y. Zhang, J. Guo, Z. Wang, H. Wang, N. Zhao, Y. Zheng, C. Du, Z. Dai, Q. Yan, J. Xu, 1D to 3D hierarchical iron selenide hollow nanocubes assembled from $FeSe_2$@C core-shell nanorods for advanced sodium ion batteries, Energy Storage Mater. 10 (2018) 48–55.
[19] L. Su, Y. Zhong, Z. Zhou, Role of transition metal nanoparticles in the extra lithium storage capacity of transition metal oxides: a case study of hierarchical core–shell $Fe_3O_4$@C and Fe@C microspheres, J. Mater. Chem. A 1 (2013) 15158–15166.
[20] Y. Yan, Y.X. Yin, Y.G. Guo, L.J. Wan, A sandwich-like hierarchically porous carbon/graphene composite as a high-performance anode material for sodium-ion batteries, Adv. Energy Mater. 4 (2014) 1301584.
[21] J. Ding, H. Wang, Z. Li, A. Kohandehghan, K. Cui, Z. Xu, B. Zahiri, X. Tan, E.M. Lotfabad, B.C. Olsen, D. Mitlin, Carbon nanosheet frameworks derived from peat moss as high performance sodium ion battery anodes, ACS Nano 7 (2013) 11004–11015.
[22] C. Zhu, Y. Wen, P.A. van Aken, J. Maier, Y. Yu, High lithium storage performance of FeS nanodots in porous graphitic carbon nanowires, Adv. Funct. Mater. 25 (2015) 2335–2342.
[23] X. Yang, Z. Zhang, Y. Fu, Q. Li, Porous hollow carbon spheres decorated with molybdenum diselenide nanosheets as anodes for highly reversible lithium and sodium storage, Nanoscale 7 (2015) 10198–10203.
[24] Y. Tang, Z. Zhao, Y. Wang, Y. Dong, Y. Liu, X. Wang, J. Qiu, Ultrasmall $MoS_2$ nanosheets mosaiced into nitrogen-doped hierarchical porous carbon matrix for enhanced sodium storage performance, Electrochim. Acta 225 (2017) 369–377.
[25] J.S. Cho, S.Y. Lee, Y.C. Kang, First introduction of $NiSe_2$ to anode material for sodium-ion batteries: a hybrid of graphene-wrapped $NiSe_2$/C porous nanofiber, Sci. Rep. 6 (2016) 23338.
[26] J.S. Cho, J.M. Won, J.-K. Lee, Y.C. Kang, Design and synthesis of multiroom-

structured transition metal compounds (oxide, sulfide, selenide)–carbon hybrid microspheres as advanced anode materials for Na- and Li-ion batteries, Nano Energy 26 (2016) 466–478.
[27] A. Ōya, S. Ōtani, Catalytic graphitization of carbons by various metals, Carbon 17 (1979) 131–137.
[28] M. Sevilla, A.B. Fuertes, Catalytic graphitization of templated mesoporous carbons, Carbon 44 (2006) 468–474.
[29] J. Li, M. Zou, L. Chen, Z. Huang, L. Guan, An efficient bifunctional catalyst of Fe/$Fe_3C$ carbon nanofibers for rechargeable Li–$O_2$ batteries, J. Mater. Chem. A 2 (2014) 10634–10638.
[30] J.H. Kim, Y.C. Kang, Synthesis of uniquely structured yolk–shell metal oxide microspheres filled with nitrogen-doped graphitic carbon with excellent Li–ion storage performance, Small 13 (2017) 1701585.
[31] J.S. Cho, H.S. Ju, J.K. Lee, Y.C. Kang, Carbon/two-dimensional $MoTe_2$ core/shell-structured microspheres as an anode material for Na-ion batteries, Nanoscale 9 (2017) 1942–1950.
[32] S. Jiang, Y. Zhang, Y. Gan, Z. Chen, H. Peng, Molecular dynamics study of neck growth in laser sintering of hollow silver nanoparticles with different heating rates, J. Phys. D 46 (2013) 335302.
[33] S.L. Che, K. Takada, K. Takashima, O. Sakurai, K. Shinozaki, N. Mizutani, Preparation of dense spherical Ni particles and hollow NiO particles by spray pyrolysis, J. Mater. Sci. 34 (1999) 1313–1318.
[34] W. Shi, X. Zhang, G. Che, W. Fan, C. Liu, Controlled hydrothermal synthesis and magnetic properties of three-dimensional $FeSe_2$ rod clusters and microspheres, Chem. Eng. J. 215 (2013) 508–516.
[35] S. Huang, Q. He, W. Chen, J. Zai, Q. Qiao, X. Qian, 3D hierarchical $FeSe_2$ microspheres: controlled synthesis and applications in dye-sensitized solar cells, Nano Energy 15 (2015) 205–215.
[36] T. Yamashita, P. Hayes, Analysis of XPS spectra of $Fe^{2+}$ and $Fe^{3+}$ ions in oxide materials, Appl. Surf. Sci. 254 (2008) 2441–2449.
[37] Y. Zeng, Y. Han, Y. Zhao, M. Zeng, Y. Yu, H. Liu, Y. Tang, X.Lu. Tong, Advanced Ti-doped $Fe_2O_3$@ PEDOT core/shell anode for high-energy asymmetric supercapacitors, Adv. Energy Mater. 5 (2015) 1402176.
[38] Q. Zheng, X. Cheng, H. Li, Microwave synthesis of high activity $FeSe_2$/C catalyst toward oxygen reduction reaction, Catalysts 5 (2015) 1079–1091.
[39] U.N. Maiti, J. Lim, K.E. Lee, W.J. Lee, S.O. Kim, Three-dimensional shape engineered, interfacial gelation of reduced graphene oxide for high rate, large capacity supercapacitors, Adv. Mater. 26 (2014) 615–619.
[40] S.T. Jackson, R.G. Nuzzo, Determining hybridization differences for amorphous carbon from the XPS C 1s envelope, Appl. Surf. Sci. 90 (1995) 195–203.
[41] D.C. Marcano, D.V. Kosynkin, J.M. Berlin, A. Sinitskii, Z. Sun, A. Slesarev, L.B. Alemany, W. Lu, J.M. Tour, Improved synthesis of graphene oxide, ACS Nano 4 (2010) 4806–4814.
[42] L. Zeng, W. Zeng, Y. Jiang, X. Wei, W. Li, C. Yang, Y. Zhu, Y. Yu, A flexible porous carbon nanofibers-selenium cathode with superior electrochemical performance for both Li-Se and Na-Se batteries, Adv. Energy Mater. 5 (2015) 1401377.
[43] H. Fan, H. Yu, X. Wu, Y. Zhang, Z. Luo, H. Wang, Y. Guo, S. Madhavi, Q. Yan, Controllable preparation of square nickel chalcogenide (NiS and $NiSe_2$) nanoplates for superior Li/Na ion storage properties, ACS Appl. Mater. Interfaces 8 (2016) 25261–25267.
[44] S. Ni, X. Yang, T. Li, Fabrication of a porous NiS/Ni nanostructured electrode via a dry thermal sulfuration method and its application in a lithium ion battery, J. Mater. Chem. 22 (2012) 2395–2397.
[45] D. Xie, Q. Su, Z. Dong, J. Zhang, G. Du, L-cysteine-assisted preparation of porous NiO hollow microspheres with enhanced performance for lithium storage, CrystEngComm 15 (2013) 8314–8319.
[46] Y. Kim, Y. Kim, Y. Park, Y.N. Jo, Y.J. Kim, N.S. Choi, K.T. Lee, SnSe alloy as a promising anode material for Na-ion batteries, Chem. Commun. 51 (2015) 50–53.
[47] X. Yan, X. Tong, J. Wang, C. Gong, M. Zhang, L. Liang, Synthesis of hollow nickel oxide nanotubes by electrospinning with structurally enhanced lithium storage properties, Mater. Lett. 136 (2014) 74–77.
[48] J.S. Cho, Y.J. Hong, Y.C. Kang, Design and synthesis of bubble-nanorod-structured $Fe_2O_3$ carbon nanofibers as advanced anode materials for Li-ion batteries, ACS Nano 9 (2015) 4026–4035.
[49] S.H. Ng, J. Wang, D. Wexler, K. Konstantinov, Z.P. Guo, H.K. Liu, Highly reversible lithium storage in spheroidal carbon-coated silicon nanocomposites as anodes for lithium-ion batteries, Angew. Chem. Int. Ed. 45 (2006) 6896–6899.
[50] S. Ameen, M.S. Akhtar, Y.S. Kim, H.S. Shin, Synthesis and electrochemical impedance properties of CdS nanoparticles decorated polyaniline nanorods, Chem. Eng. J. 181 (2012) 806–812.
[51] S.J. Patil, J.H. Kim, D.W. Lee, Self-assembled $Ni_3S_2$//$CoNi_2S_4$ nanoarrays for ultra high-performance supercapacitor, Chem. Eng. J. 322 (2017) 498–509.
[52] S. Abureden, F.M. Hassan, G. Lui, W. Ahn, S. Sy, A. Yu, Z. Chen, Multigrain electrospun nickel doped lithium titanate nanofibers with high power lithium ion storage, J. Mater. Chem. A 4 (2016) 12638–12647.
[53] W. Wang, W. Liu, Y. Zeng, Y. Han, M. Yu, X. Lu, Y. Tong, A novel exfoliation strategy to significantly boost the energy storage capability of commercial carbon cloth, Adv. Mater. 27 (2015) 3572–3578.